

This is an Open Access document downloaded from ORCA, Cardiff University's institutional repository:<https://orca.cardiff.ac.uk/id/eprint/144575/>

This is the author's version of a work that was submitted to / accepted for publication.

Citation for final published version:

Jia, Zhiyong, Rondiya, Sachin R., Cross, Russell W., Wang, Cheng, Dzade, Nelson Y. and Zhang, Chuang 2021. Highly active methanol oxidation electrocatalyst based on 2D NiO porous nanosheets: a combined computational and experimental study. *Electrochimica Acta* 394 , 139143. 10.1016/j.electacta.2021.139143

Publishers page: <http://dx.doi.org/10.1016/j.electacta.2021.139143>

Please note:

Changes made as a result of publishing processes such as copy-editing, formatting and page numbers may not be reflected in this version. For the definitive version of this publication, please refer to the published source. You are advised to consult the publisher's version if you wish to cite this paper.

This version is being made available in accordance with publisher policies. See <http://orca.cf.ac.uk/policies.html> for usage policies. Copyright and moral rights for publications made available in ORCA are retained by the copyright holders.



# **Highly Active Methanol Oxidation Electrocatalyst based on 2D NiO Porous Nanosheets: A Combined Computational and Experimental Study**

Zhiyong Jia<sup>a</sup>, Sachin R. Rondiya<sup>b</sup>, Russell W. Cross<sup>b</sup>, Cheng Wang<sup>c</sup>,

Nelson Y. Dzade<sup>b\*</sup>, Chuang Zhang<sup>a,c\*</sup>

<sup>a</sup>School of Automobile and Traffic Engineering, Hubei University of Arts and Science, Xiangyang 441058, P. R. China.

<sup>b</sup>School of Chemistry, Cardiff University, Main Building, Park Place, Cardiff, CF103AT, Wales, United Kingdom.

<sup>c</sup>Zhang Jiagang Joint Institute for Hydrogen Energy and Lithium-Ion Battery Technology, INET, Tsinghua University, Beijing 100000, P. R. China.

Corresponding author:

Nelson Y. Dzade ([dzadeny@cardiff.ac.uk](mailto:dzadeny@cardiff.ac.uk));

Chuang Zhang ([zhangchuang@tsinghua.edu.cn](mailto:zhangchuang@tsinghua.edu.cn))

## Abstract

Two-dimensional (2D) nanostructures are attractive candidates for electrocatalytic applications owing to their excellent mechanical flexibility and large exposed surfaces. In this work, we present ultra-thin 2D NiO porous nanosheets prepared by a simple, economical and green experimental method (hydrothermal, freeze-drying, and sintering) as efficient electrocatalysts for direct methanol fuel cell (DMFC) application. Benefiting from the ultra-thin 2D framework and porous nanostructure, the 550-NiO catalyst (annealed at 550 °C) exhibit higher current density ( $12.54\text{mA cm}^{-2}$ ) and faster charge transfer in the catalytic process, due to its abundant solid state redox couples ( $\text{Ni}^{2+}/\text{Ni}^{3+} = 0.991$ ), suitable oxygen defects and surface coverage of redox species ( $2.90 \times 10^{-7} \text{mol cm}^{-2}$ ). First-principles density functional theory calculations were employed to provide mechanistic insights into the methanol oxidation reaction over the NiO catalyst via methanol dehydrogenation to CO involving O–H and C–H bond scissions, and subsequently, CHO oxidation with OH. The most plausible reaction pathway of methanol oxidation on NiO (100) is predicted to be  $\text{CH}_3\text{OH} \rightarrow \text{CH}_3\text{O} \rightarrow \text{CH}_2\text{O} \rightarrow \text{CHO} \rightarrow \text{CHOOH} \rightarrow \text{COOH} \rightarrow \text{CO}_2$ . The reported facile, simple, low-cost and method provides an avenue for the rational design and synthesis of 2D NiO porous nanostructured electrode materials for DMFC and beyond.

**Keywords:** Methanol oxidation reaction; Nickel oxide; Electrocatalyst; Density functional theory; Direct methanol fuel cell.

## 1. Introduction

Direct methanol fuel cells (DMFC) have attracted much attention due to their small size, convenient fuel use, clean environment protection and high theoretical energy ratio. To improve the DMFC efficiency and performance, highly efficient and low cost catalytic materials for methanol oxidation are of great importance. Currently, Pt or Pt alloys (e.g. Pt/Ru, Pt/Ru/Ni, Pt/Co, Pt/Sn)[1-5] are the most popular catalysts for DMFC, but the high cost of Pt catalysts, slow kinetic oxidation, and the formation of CO intermediate molecules during the methanol oxidation reaction severely limit their widespread application. The poor catalytic kinetic performance is mainly due to the unstable structure of existing catalysts, less active sites, small specific surface area, serious agglomeration of nanoparticles and a slow ion migration rate. Therefore, a great deal of effort has to be made towards the rational design and synthesis of cost-effective and earth-abundant catalysts as possible alternatives to precious metal catalysts.

Transition metal oxides such as  $\text{Co}_3\text{O}_4$ ,  $\text{TiO}_2$ ,  $\text{MnO}_2$ ,  $\text{NiO}$ ,  $\text{SnO}_2$ ,  $\text{V}_2\text{O}_5$ , etc., which can be prepared in various nanostructured forms (nanorod, nanoparticle, and nanosheets) have received considerable attention. Hexagonal  $\text{NiO}$ , an important member of transition metal oxides, has been widely used as an electrocatalyst for oxygen reduction reaction (ORR), oxygen evolution reaction (OER) and hydrogen evolution reaction (HER). They are also attractive for energy storage applications (e.g. supercapacitors, and lithium ion batteries). However, there exist limited studies on methanol oxidation reaction (MOR) catalyzed by  $\text{NiO}$ . Recent reports have focused on composites of  $\text{NiO}$  and other materials such as  $\text{CeO}_2$  [6], Ni foam [7], carbon nanofibers [8], CNT[9-11], mesoporous carbon[12], and graphene[13]. According to the literature, the improvement of the catalytic performance of pure  $\text{NiO}$  catalysts can be achieved through: (1) obtaining excellent nanostructures or channels by optimizing the synthesis; and (2) improving the distribution of different valence ions on the surface of materials and obtaining appropriate oxygen defects by changing the synthesis conditions.

It is common to design different nanostructures to improve MOR activity.  $\text{NiO}$  nanotubes [14], porous film [15], nanofibers [16], and flower-like structures [17, 18] have been developed. Ultra-thin two-dimensional (2D) nanosheets with large specific

surface area can provide effective sites and excellent ion transport channels for catalytic processes, which is beneficial for the adsorption of reactants, the permeation of electrolyte and, hence, the acceleration of reaction kinetics. In alkaline medium, Ni will provide active sites for solid state redox couples, which are  $\text{Ni}^{2+}/\text{Ni}^{3+}$  in NiO. The richer the redox couples, the higher the catalytic activity. However, there are few reports on the evaluation of the catalytic activity of  $\text{Ni}^{2+}/\text{Ni}^{3+}$  abundance in NiO catalysts. On the other hand, oxygen defects are also an important index to evaluate the catalytic activity of NiO. The contribution of oxygen defects in methanol oxidation still needs further study.

In this study, ultra-thin 2D porous self-supporting NiO nanosheets were designed and synthesized with a simple, green and economic approach. We quantified the  $\text{Ni}^{2+}/\text{Ni}^{3+}$  ratio, which provides a descriptor of the catalytic active sites in pure NiO, and studied the role of oxygen defects in the catalytic process. It provides the foundation for the design, synthesis and theoretical research of transition metal oxide catalysts.

## **2. Experimental**

### **2.1 Preparation of NiO catalysts**

The NiO catalysts were prepared through the following steps. Step 1: add 2 g  $\text{NiSO}_4 \cdot 6\text{H}_2\text{O}$  into 50 mL deionized water, stir with glass rod for 10 minutes, and then ultrasonic disperse for 10 minutes. Step 2: 3 mL of  $\text{NH}_3 \cdot \text{H}_2\text{O}$  (30 v/v %) was slowly added into the above mixed solution, and then put into the Teflon for reaction at 50 °C for 48 hours. Step 3: clean the NiO precursor with an excess of deionized water and freeze-dry (deep well temperature is -60 °C, and the sample placement temperature is 16 °C) for 24 hours to obtain NiO precursor. Step 4: the NiO precursor was tested under a range of annealing temperatures (350, 450, 550, 650°C) in air to obtain four different catalysts, named 350-NiO, 450-NiO, 550-NiO and 650-NiO, respectively.

### **2.2 Physical characterizations**

PHILIPS XL30TMP was used to perform scanning electron microscopy (SEM) and a Titan G2 60-300 high resolution transmission electron microscopy (HRTEM). The

selected area electron diffraction (SAED) pattern was used to characterize the NiO catalysts and the change of morphology and crystal structures after annealing at different temperatures. The thermogravimetric analysis (TGA) was carried out on an SDTQ 600, from 20 to 800 °C and a heating rate of 10 °C min<sup>-1</sup>. X-ray diffraction (XRD) data of the synthesized powder samples were detected in BrukerD8 (Cu K $\alpha$  radiation). The valence states and content changes of Ni, O elements on the samples surface were characterized by X-ray photoelectron spectra (XPS, ESCALAB250Xi). The surface area and pore size of the sample were analyzed by Nitrogen adsorption/desorption isotherms (MicroActive for ASAP 2460 2.01).

### **2.3 Electrochemical measurements**

Princeton electrochemical workstation (PMC-2000) was used for the electrochemical test. The three electrode system consisting of a working electrode (glassy carbon with an area of 0.07065 cm<sup>2</sup>, WE), reference electrode (Ag/AgCl) and counter electrode (Pt tablet). The catalyst slurry is formed by adding 5 mg of catalyst to 950  $\mu$ L isopropanol and 50  $\mu$ L Nafion (5 wt%, DuPont) mixture for ultrasonic dispersion for more than 2 hours. The 5  $\mu$ L slurry is dripped onto the surface of the WE using a microinjector and allowed to dry. 0.1 mol L<sup>-1</sup> KOH solution was used as the electrolyte for the three electrode system. The cyclic-voltammetry (-0.2 V to 1.0 V, CV) of methanol oxidation was carried out in saturated nitrogen with a scanning rate of 50 mV s<sup>-1</sup> and under a methanol concentration of 0.01, 0.02, 0.05, 0.1, 0.2, 0.5, 1.0, 2.0, 3.0, 4.0 and 5.0 mol L<sup>-1</sup>, respectively. The sweep rate of CV used to calculate the surface coverage is 1 mV s<sup>-1</sup> to 500 mV s<sup>-1</sup>, and the sweep potential range is 0- 1.0 V.

### **2.4 Details of density functional theory (DFT) calculation**

The density functional theory (DFT) calculations were carried out within the Vienna Ab initio Simulation Package (VASP) [19-21] with the exchange-correlation functional of Perdew–Burke–Ernzerhof (PBE) [22]. The interactions between the core and valence electrons were treated using the Project Augmented Wave (PAW) method [23]. The electronic wave functions are expanded on a plane-wave basis set with a cutoff energy of 600 eV. Geometry optimization was carried out using the conjugate-gradient

algorithm ensuring that the residual Hellmann–Feynman forces on all relaxed atoms reached  $10^{-3}$  eV/Å. Long-range vdW interactions were accounted for using the GrimmeDFT-D3 scheme.[24] To overcome the limitation of standard DFT methods in accurately predicting the electronic bandgap and magnetic properties of semiconducting materials, the DFT+U method [25, 26] was employed (an effective U of 7 eV is found to accurately predict the electronic and magnetic properties of hexagonal (R-3m) NiO). The bulk NiO was modeled in the hexagonal (R-3m) structure with antiferromagnetic spin ordering. A  $9 \times 9 \times 5$  Monkhorst-Pack  $k$ -point mesh used to sample the Brillouin zone. The NiO (100) surface, created using the METADISE code[27], was used to characterize the adsorption of methanol and its dehydrogenation reactions because it is predicted as the most stable surface among the three surfaces ((100), (110) and (111)) investigated. The (100) surface has a low surface energy of  $1.43 \text{ Jm}^{-2}$  compared to  $1.78 \text{ Jm}^{-2}$  for the (110) surface. For the (111) surface, because it has equidistant alternating layers of oppositely charged ions, it has a large dipole moment perpendicular to the surface. By reconstructing the (111) surface to fulfil the polarity compensation criteria,[28, 29] it was found to have a surface energy of  $1.59 \text{ Jm}^{-2}$ , which is higher than that of the (100) surface. Owing to the predicted stability of the (100) surface, it is expected to be the most expressed and abundant facet in hexagonal NiO nanocrystal. Transition states (TS) along reaction pathways were determined using the climbing-image nudged elastic band (CI-NEB) method, [30] wherein, six images were generated between the states of reactants (IS) and products (FS) in each elementary process. Identified transition states were further confirmed through vibrational frequency calculation, where only one imaginary frequency was obtained, corresponding to the reaction coordinate. The reaction activation energy barrier ( $E_A$ ) is determined by  $E_a = \text{TS} - \text{IS}$ , whereas the reaction energy ( $\Delta E$ ) is determined by  $\Delta E = \text{FS} - \text{IS}$ .

### **3. Results and discussion**

#### **3.1 Morphology and structure characterizations**

Shown in Fig. 1 is a schematic diagram of the process of synthesizing NiO. The aqueous solution of NiSO<sub>4</sub> is a homogeneous green solution (Fig. 1 a). A green precipitate is formed after hydrothermal reaction (Fig. 1 b). After freeze-drying, the green NiO precursor is formed by stacking two-dimensional (2D) sheets (Fig. 1 c). After annealing in air at different temperatures to form black 2D NiO nanosheets, the nanosheets remain intact at low temperatures (Fig. 1 d); at 550 °C, they can maintain the general shape of the flakes, but there will be obvious porous holes structure (Fig. 1 e); when the temperature reaches 650 °C, the 2D NiO nanosheets almost became fragmented as shown in Fig. 1 f. SEM shows the NiO precursor and the four NiO samples in Fig. 2. The 2D nanosheet-shaped NiO precursors (Fig. 2 a and b) are stacked together and there is large space between layers. The thickness of this ultra-thin sheet is about few nanometers. NiO-350 (Fig. 2 c and d) and NiO-450 (Fig. 2 e and f) show the same 2D nanosheet-shapes however each sheet is composed of smaller NiO nanoparticles. NiO-550 (Fig. 2 g and h) presents a unique porous 2D plate-like structure, indicating that as the temperature increases, the NiO particles grow up, and the nano-sheets are subjected to increased internal stresses, resulting in holes. The appearance of these holes is conducive to the transmission of gas, ions and electrolyte. However, when the temperature increased to 650 °C (Fig. 2 i and j), the NiO sheet structure collapsed, and the NiO particle formation rapidly increased, resulting in fragmentation of the 2D NiO nanosheets.

TEM and HR-TEM show in Fig. 3. Very thin nanosheets are observed in the 350-NiO and 450-NiO samples ( Fig.3a and c) and lattice resolved structure analyses reveal clear lattice fringes with *ad*-spacing of about 0.24 nm and 0.21 nm, which represent the (1 1 1) and (2 0 0) planes of the NiO, respectively [31, 32]. At the same time, a small number of holes have appeared in 450-NiO, with diameters ranging from 5 to 20 nm. A large number of holes also appear in 2D nanosheets of the 550-NiO, and the diameter of the holes' ranges from 50 to 150 nm as shown in Fig.3e. The crystalline structure (Fig.3f) having *d*-spacing of about 0.24 nm means the (1 1 1) plane of the NiO is present. The SAED pattern is shown as inset in Fig.3f [33]. When the annealing temperature reaches 650 °C, it can be seen in Fig.3g that the 650-NiO sample becomes a fragmented



structure. And crystalline structure (Fig.3h) having  $d$ -spacing about 0.24 nm can be assigned to the (1 1 1) plane.

As shown in Fig. 4a, the TGA revealed that the mass loss before 283 °C, which can be attributed the loss of free water in the sample. More than 11.0% weight loss between 283°C and 330 °C is mainly due to the elimination of hydroxyl groups by evaporation of water molecules [31]. The XRD spectra of the samples are shown in Fig.4b. For the NiO-precursor, the XRD peaks can be assigned to the pure hexagonal phase of Ni(OH)<sub>2</sub> [31]. For 350-NiO, 450-NiO, 550-NiO and 650-NiO, the peaks at  $2\theta \approx 38.1^\circ$ ,  $43.7^\circ$ , and  $63.3^\circ$  correspond to the (1 1 1), (2 0 0) and (2 2 0) characteristic planes of the NiO product. In particular, basal reflections peaks appear at  $27.0^\circ$  and  $52.0^\circ$ , which shows the 2D ordering of the NiO nanosheet.

To gain further insights into the surface chemical composition of the NiO materials, XPS analysis was carried out. It can fit the composition peaks of Ni 2p and O 1s by using Gaussian fitting method as shown in Fig.S1 and Fig.S2, respectively. The Ni 2p spectra can be deconvoluted at the binding energy (BE) of 853.8, 855.5, 861.1, 871.9, 873.8 and 879.5 eV [34, 35]. The peaks at BE of 853.8 and 871.9 eV can be ascribed to Ni<sup>2+</sup>, whereas those at BE of 855.5 and 873.8 eV can be assigned to Ni<sup>3+</sup>. The satellite peaks appear at BE of 879.5 and 861.1 eV. It is difficult to calculate the contribution of Ni<sup>2+</sup> and Ni<sup>3+</sup> in the satellite peak of Ni 2p spectrum, so it is not included in the calculation process. The ratio of Ni<sup>2+</sup>/Ni<sup>3+</sup> can be obtained by calculating the integral area ratio of Ni<sup>2+</sup> and Ni<sup>3+</sup> as shown in Fig.4c. The ratios of Ni<sup>2+</sup>/Ni<sup>3+</sup> in 350-NiO, 450-NiO, 550-NiO and 650-NiO catalysts are 0.819, 0.864, 0.991 and 1.157, respectively. The catalytic activity of NiO depends on the surface of solid state redox couples (SSRC).[36, 37] In the NiO catalyst, the Ni<sup>2+</sup>/Ni<sup>3+</sup> constitute the SSRC, which is a charge transfer channel in the catalytic oxidation process. The closer Ni<sup>2+</sup>/Ni<sup>3+</sup> ratio is to 1, the more abundant the SSRC and the more active sites. Comparing the four catalysts, the ratio of Ni<sup>2+</sup>/Ni<sup>3+</sup> in 550-NiO is closest to 1, suggesting that NiO sample annealed at 550 °C has the most abundant SSRC. The O 1s spectra deconvolution at BE of 529.7 eV, 531.5 eV, and 532.8 eV, correspond to the metal oxygen bonds (M-O), low coordination surface oxide ions (O<sup>2-</sup>), and hydroxyl groups (chemisorbed oxygen).

Combined with the distribution of oxygen components in different samples as shown in Fig.4d, it can be seen that the different species of oxygen also changes significantly with increase in the sintering temperature: the content of  $O^{2-}$  species was the highest at 350 °C, but gradually decreased with increased sintering temperature. On the contrary, the oxygen content in the M-O covalent bond increases with the temperature. These results are consistent with the ratio change of  $Ni^{2+}/Ni^{3+}$  with the increase of temperature, as shown in Fig.4c. Based on the above data, the evolution process of various oxygen species included in the crystal during the nickel hydroxide sintering process can be explained: at lower sintering temperature (350 °C), a large number of hydroxyl groups contained in the nickel hydroxide are formed through pyrolysis and are removed by means of the water molecule at 300 °C (TGA data in Fig.4a), producing a large number of unstable  $O^{2-}$  ions inside the crystals. Although the concentration of  $Ni^{3+}$  ions is also higher in the crystal, the unstable  $O^{2-}$  ions dimerizes to form  $O_2$ , which escapes from the crystal and leaves many oxygen holes in the crystal as the temperature continues to rise. As a result, the concentration of  $Ni^{3+}$  began to decrease, contrasted with the increased concentration of  $Ni^{2+}$ . As the temperature goes up, the ratio of  $Ni^{2+}/Ni^{3+}$  and the oxygen species forming M-O covalent bonds keeps going up with the increased  $Ni^{2+}$ . In short, the higher the annealing temperature, the more oxygen defects are created in the catalyst structure.

Shown in Fig.4e is the  $N_2$  adsorption-desorption isotherms of the four catalysts, which give further insights about the surface structure. The surface area of 350-NiO, 450-NiO, 550-NiO and 650-NiO are estimated at 103.7, 51.5, 26.1 and 17.9  $m^2 g^{-1}$ , respectively. The BET surface area of 350-NiO is twice that of 450-NiO and nearly 4 times that of 650-NiO, which indicates that the surface area decreases sharply with the increase of annealing temperature.

### 3.2 Analysis of methanol electro-oxidation

The catalytic mechanism of NiO for methanol oxidation is as follows [32, 34, 38, 39]:





Equations (1-a) and (2-a) reveal the mutual transformation between  $\text{Ni}^{2+}$  and  $\text{Ni}^{3+}$ , providing SSRC.

Fig.S3 (a and b) show the methanol oxidation CV at different methanol concentrations for 350-NiO catalyst. The catalytic activity of 350-NiO increases first and then decreased with increasing of methanol concentration: the optimum activity is reached at methanol concentration of  $0.05 \text{ mol L}^{-1}$ . The corresponding current density of methanol oxidation peak for 350-NiO catalyst is shown in Fig.S3c. The methanol oxidation CV of the 450-NiO, 550-NiO, and 650-NiO catalysts at different methanol concentrations are shown in Fig.S4a and b, Fig.S5 a and b, Fig.S6 a and b, respectively. The optimal methanol concentration for the 450-NiO, 550-NiO, and 650-NiO catalysts is obtained at  $0.2$ ,  $1.0$ , and  $1.5 \text{ mol L}^{-1}$ , respectively. The curves of methanol oxidation peak current density with methanol concentration for the 450-NiO, 550-NiO, and 650-NiO catalysts are shown in Fig.S4c, Fig.S5c and Fig.S6c.

Comprehensive analysis of methanol oxidation peak current density with methanol concentration curve is shown in Fig. 5a. It can be seen that the catalytic performance trend is  $350\text{-NiO} > 450\text{-NiO} > 550\text{-NiO} > 650\text{-NiO}$  at low methanol concentration as shown in Fig.5b ( $0.05 \text{ mol L}^{-1}$ ). It is mainly because the methanol concentration is very low in the catalytic process, namely “starvation” state, and 350 has the highest specific surface area at this time, so more methanol molecules can be adsorbed to participate in the catalytic process. The specific surface area plays a decisive role in the catalyst process at low methanol concentration. When methanol concentration increased to medium concentration, the catalytic activity trend is  $550\text{-NiO} > 350\text{-NiO} > 450\text{-NiO} > 650\text{-NiO}$  as shown in Fig.5c ( $0.20 \text{ mol L}^{-1}$ ). With an increase of methanol concentration, the catalytic activity of 550-NiO increases rapidly. When the concentration of methanol reaches  $0.1 \text{ mol L}^{-1}$ , the catalytic activity of 550-

NiO is higher than the other three catalysts. It is mainly related to its stable porous structure and abundant SSRC ( $\text{Ni}^{2+}/\text{Ni}^{3+}=0.991$ ). Interestingly, when the methanol concentration reaches  $1.0 \text{ mol L}^{-1}$ , the activity of the catalyst changes to  $550\text{-NiO} > 650\text{-NiO} > 450\text{-NiO} > 350\text{-NiO}$  as shown in Fig.5d (the maximum oxidation peak of methanol is determined by the intersection of two tangents when the CV curve changes, as shown in Fig. 5d of 450-NiO). At this time, methanol is “saturated”. The catalytic activity depends on many factors, such as specific surface area, SSRC and catalyst structure. 350-NiO has the highest specific surface area and can adsorb more methanol molecules, but its SSRC is the lowest, which can not provide effective catalytic active sites in the catalytic process. On the contrary, 550-NiO has the most abundant SSRC and stable porous structure, so its catalytic activity is always the best. The lower catalytic activity of 650-NiO than 550-NiO is due to its smaller SSRC and fragmented structure. However, 650-NiO is better than 450-NiO and 350-NiO because it retains partial pore structure and maximum oxygen defects (Fig.4 c and d). At the same time, high oxygen defects will lead to the interaction of defect-defect, resulting in the reduction of catalytic activity [40]. This may be one of the reasons why the catalytic activity of 650-NiO is lower than that of 550-NiO.

In order to evaluate the surface coverage of redox species (SCRS) on the catalyst surface, the following formula is used:

$$I_p = vAC^* \frac{n^2 F^2}{4RT} \quad (3)$$

where  $I_p$  is the measured peak current density of the catalysts,  $v$  the potential sweep rate ( $\text{V s}^{-1}$ ),  $A$  the area of the working electrode,  $C^*$  the surface coverage of the redox species ( $\text{mol cm}^{-2}$ ), and  $n$  is the number of transferred electrons.  $R$  ( $8.314 \text{ J K}^{-1}$ ) and  $F$  ( $96500 \text{ C mol}^{-1}$ ) are constants.

By fitting the current density of oxidation and reduction peak at sweep speed less than  $20 \text{ mV}$  (saturated  $\text{N}_2$ ), the obtained results for the 350-NiO, 450-NiO, 550-NiO, and 650-NiO catalysts are shown in Fig.S3e, Fig.S4e, Fig.S5e and Fig.S6e, respectively. The results show that the average SCRS for the 350-NiO, 450-NiO, 550-NiO and 650-NiO catalysts is  $2.90 \times 10^{-6}$ ,  $1.33 \times 10^{-6}$ ,  $2.90 \times 10^{-7}$ , and  $1.38 \times 10^{-7} \text{ mol cm}^{-2}$ , respectively.

These results suggest that higher annealing temperatures of the NiO catalyst, leads to lower SCRS, which may be related to the specific surface area.

Through the above analysis, 550-NiO is demonstrated to give the best catalytic activity; the performance diagram of the SSRC and methanol electrocatalysis at 1.0 mol L<sup>-1</sup> is obtained, as shown in Fig.6. It shows that the richer the SSRC (Ni<sup>2+</sup>/Ni<sup>3+</sup> is close to 1), the better the catalytic performance. The higher catalytic activity of 550-NiO is attributed to its stable porous 2D nanosheets (Fig.2g and Fig.3e), abundant SSRC (Fig.4c) on the surface and oxygen defects (Fig.4d) in the structure. Methanol molecules are adsorbed on the surface of 2D NiO nanosheets, and Ni ions can catalyze the oxidation of methanol molecules through valence change. At the same time, referring to the BET surface area, although larger BET surface area can provide more reactive active sites, the improvement of performance after 500 °C annealing is related to richer SSRC.

### 3.2 First-principles DFT calculations

Detailed mechanistic insight into the oxidation reactions of methanol on the NiO catalyst was gained from first-principles DFT calculations. Firstly, the structural parameters and the electronic structure of NiO was determined as shown in Fig.7 (a & b). The lattice parameters of the hexagonal (R-3m) NiO are predicted at  $a=b= 2.956 \text{ \AA}$ , and  $c= 7.183 \text{ \AA}$ , all in good agreement with the experimental estimates of  $a=b=2.955 \text{ \AA}$ , and  $c= 7.226 \text{ \AA}$ . The partial density of states (Fig. 7b) reveals that O-*p* states dominate the valence band, whereas Ni-*d* states dominate the conduction band edge. The band gap is predicted at 3.56 eV, in close agreement with previous experimental[41, 42] and DFT[43] results.

Shown in Fig. 7c is the relaxed structure of the NiO (100) surface employed to characterize the adsorption geometries and energies for methanol and various intermediates along the reaction pathway of methanol oxidation. The lowest-energy adsorption configurations of CH<sub>3</sub>OH, CH<sub>3</sub>O, CH<sub>2</sub>O, CHO, and CO are shown in Fig. 8, with the corresponding adsorption energies and interatomic bond distances summarized in Table S1. CH<sub>3</sub>OH is found to preferentially adsorb at Ni-top site on NiO

(100) through its oxygen atom with the Ni–O distance of 2.01 Å (Fig. 8a). The adsorption energy of CH<sub>3</sub>OH is predicted at –2.14 eV. The closest H–O<sub>surf</sub> distance is calculated at 1.823 Å, indicating that hydrogen-bond interactions contributed to the stabilisation of methanol on NiO (100) surface. Consistently, the O–H bond is slightly elongated (1.017 Å) relative the gas phase methanol bond length of 0.971 Å. Methoxy specie (CH<sub>3</sub>O), which can be formed from O–H activation of methanol adsorbs at top-Ni site ( $d_{\text{Ni-O}} = 1.743$  Å), releasing an adsorption energy of –2.42 eV. C–H activation of methanol may form hydroxymethyl (CH<sub>2</sub>OH), which is found to adsorb at adjacent Ni-top sites through the C ( $d_{\text{C-Ni}} = 1.937$  Å) and O ( $d_{\text{O-Ni}} = 2.019$  Å) atoms, releasing an adsorption energy of –2.25 eV. Formaldehyde (CH<sub>2</sub>O) adsorbs flat on the surface with the O and C atoms binding at adjacent Ni-top sites (with  $d_{\text{O-Ni}} = 1.841$  Å and  $d_{\text{C-Ni}} = 1.982$  Å), releasing an adsorption energy of –1.79 eV. Like formaldehyde, the formyl (CHO) adsorbs with the C–O axis parallel to the NiO (100) surface, binding via O–Ni (1.872 Å) and C–Ni (1.813 Å) bonds. Consistent with the shorter C–Ni bond, CHO adsorbs strongly on the NiO (100) surface, releasing adsorption energy of –3.79 eV. Carbon monoxide (CO) binds in an upright geometry via the C atom at bridge Ni-Ni site ( $d_{\text{C-Ni}} = 1.872$  Å) as shown in Fig. 8e. A much stronger adsorption (–4.20 eV) is predicted for CO on the NiO (100) surface.

Formic acid (CHOOH) adsorbs preferentially in a flat geometry (Fig. 8g), wherein the three atoms (C, O, and O) binds to adjacent top-Ni sites, releasing an adsorption energy of –2.85 eV. The two  $d_{\text{O-Ni}}$ , and  $d_{\text{C-Ni}}$  distances are predicted at 1.889, 2.075, and 2.122 Å, respectively. COOH adsorbs stably at adjacent top-Ni sites through its C and O<sub>carbonyl</sub> atoms ( $d_{\text{C-Ni}} = 1.851$  Å and  $d_{\text{O-Ni}} = 1.908$  Å), releasing adsorption energy of –2.33 eV (see Table S1). As shown in Fig. 8i, formate (HCOO) adsorbs at adjacent top-Ni sites through both O atoms (average  $d_{\text{O-Ni}} = 1.892$  Å). The adsorption energy is calculated to be –1.88 eV. CO<sub>2</sub> forms bidentate geometry at Ni-top sites (Fig. 8j), binding through the C and O atoms ( $d_{\text{O-Ni}} = 1.893$  Å and  $d_{\text{C-Ni}} = 1.919$  Å), releasing an adsorption energy of –2.18 eV. H<sub>2</sub>O adsorbs preferentially at top-Ni site via the O atom ( $d_{\text{O-Ni}} = 2.015$  Å) with adsorption energy of –1.20 eV, whereas OH adsorbs adsorb most stably at bridge Ni<sub>2</sub>-site (average  $d_{\text{O-Ni}} = 1.937$  Å) with adsorption energy of –4.54

eV. Atomic H adsorbs most favourably at top-O site ( $d_{\text{O-H}} = 0.976 \text{ \AA}$ ) releasing adsorption energy of  $-1.19 \text{ eV}$ .

Methanol decomposition may proceed via the O–H or C–H bond scissions, with the initial C–O bond scission generally too hard to occur. To ascertain which route is thermodynamically and kinetically more favoured for methanol decomposition on NiO (100) surface, the reaction energy ( $\Delta E$ ) and activation energy barrier ( $E_a$ ) for the initial O–H and C–H bond scission were computed. The  $\Delta E$  and  $E_a$  for initial O–H bond scission is calculated at  $-0.27$  and  $0.54 \text{ eV}$ , respectively, compared to  $-0.05$  and  $0.86 \text{ eV}$  for the initial C–H bond scission. The more favourable  $\Delta E$  and lower  $E_a$  predicted for initial O–H bond scission, suggests that the decomposition of methanol over the NiO (100) surface will preferentially proceed via the O–H scission route. This is consistent with previous studies that show that methanol decomposition proceeds preferably through the initial O–H scission on Cu (111) [44], Ru (0001) [44], and PtZn (111) [45].

The optimized structures for the most stable methanol decomposition intermediates, and their corresponding dissociation product species and transition states are shown in Fig. 9. The reaction energies ( $\Delta E$ ) and activation energy barriers ( $E_a$ ) are summarized in Table S2. The  $\text{CH}_3\text{O} \rightarrow \text{CH}_2\text{O} + \text{H}$  reaction is exothermic by  $-1.27 \text{ eV}$  with an activation energy barrier of  $0.90 \text{ eV}$ . The dissociated H binds to O-top site and the C atom binds at adjacent Ni-top site. Further dissociation of a C–H bond from  $\text{CH}_2\text{O}$  resulted in the formation of CHO and atomic H with the  $\Delta E$  and  $E_a$  calculated at an  $-1.05$  and  $0.84 \text{ eV}$ , respectively. For the  $\text{CHO} \rightarrow \text{CO} + \text{H}$  reaction, the  $\Delta E$  and  $E_a$  calculated at  $-1.24$  and  $0.73 \text{ eV}$ , respectively. This process involves the breaking of the Ni–O bond, followed by the movement of the C atom towards bridge Ni–Ni sites, forming a Ni–CO–Ni structure. Shown in Fig. 10 is the energy profile for methanol dehydrogenation reaction on the NiO (100) surface.

Considering that the intermediates of methanol decomposition can react with OH species formed by water activation, we have also elucidated the adsorption and dissociation of water on NiO (100) surface followed by the reaction of CHO intermediate with OH. As shown in Fig. 8k,  $\text{H}_2\text{O}$  preferentially binds at Ni-top site via

the oxygen atom ( $d_{\text{Ni-O}} = 2.015 \text{ \AA}$ ). The dissociation of one of the O–H bonds is found to be exothermic by  $-1.38 \text{ eV}$  with an activation barrier of  $0.52 \text{ V}$ , indicating that it is easy to form the OH species on the NiO (100) surface. The dissociated H atom migrated to the adjacent top-O site forming surface hydroxyl ( $\text{OH}^-$ ) species. The reaction of OH with CHO (Fig. 11a) resulted in the formation of formic acid ( $\text{HCOOH}$ ) with the  $\Delta E$  and  $E_a$  calculated  $+0.19$  and  $0.58 \text{ eV}$ , respectively. The dehydrogenation of  $\text{HCOOH}$  via the C–H scission formed bidentate COOH on NiO (100) surface (Fig. 11b), with the interacting  $d_{\text{Ni-O}}$  and  $d_{\text{Ni-C}}$  bond distanced calculated at  $1.896$  and  $1.853 \text{ \AA}$ , respectively. This dehydrogenation process has an activation energy barrier of  $0.72 \text{ eV}$  and a reaction energy of  $-0.79 \text{ eV}$ . Further dehydrogenation of the COOH specie resulted in the formation of  $\text{CO}_2$  and  $2\text{H}$  species (Fig. 11c), with the  $\text{CO}_2$  bound via Ni–O ( $1.895 \text{ \AA}$ ) and Ni–C ( $1.905 \text{ \AA}$ ) bonds, whereas the H atoms are bound to top-O sites at  $\text{H-O}_{\text{surf}}$  bond distance of  $0.978 \text{ \AA}$ . This process is exothermic by  $-0.31 \text{ eV}$  and has to overcome an activation energy barrier of  $0.68 \text{ eV}$ . We have also investigated the other possible dehydrogenation pathway of  $\text{HCOOH}$  via the O–H bond scission. The transfer of H to top-O site resulted in rotation of the CHOO species to bind via the two O atoms at adjacent Ni sites (average  $d_{\text{Ni-O}} = 1.896 \text{ \AA}$ ) as shown in Fig. 11d. This reaction is exothermic by  $-1.21 \text{ eV}$  and has an activation energy barrier of  $1.16 \text{ eV}$ . The formed HCOO specie can undergo further dehydrogenation through breaking of the O–H bond to form  $\text{CO}_2$  and  $2\text{H}$  species with a barrier of  $0.97 \text{ eV}$  and an energy change of  $1.13 \text{ eV}$  (endothermic). The  $\text{CO}_2$  molecule forms bidentate Ni–O bonds ( $2.001 \text{ \AA}$ ) whereas the H atoms bind at top-O sites ( $\text{H-O}_{\text{surf}} = 0.976 \text{ \AA}$ ).

#### 4. Conclusions

A simple, economical and green experimental method (hydrothermal, freeze-drying and sintering) has been used to obtain unique 2D nanosheets structure NiO catalyst. It was demonstrated that under low methanol concentration ( $\leq 0.05 \text{ mol L}^{-1}$ ), the specific surface area plays a decisive role in the catalyst activity. In the range of  $0.05\text{-}0.2 \text{ mol L}^{-1}$  methanol concentration, the specific surface area, structure and SSRC of the catalyst are shown to be the main factors that dictate the activity of the catalyst. When the methanol concentration  $>0.2 \text{ mol L}^{-1}$ , the catalytic activity of the catalyst mainly



depends on the abundance of SSRC and the stability of the 2D porous nanosheets. The 550-NiO catalyst (annealed at 550 °C) was demonstrate to possess a unique and perfect 2D porous nanosheet structure, and abundant SSRC ( $\text{Ni}^{2+}/\text{Ni}^{3+} = 0.991$ ) and oxygen defects. When the concentration of methanol reached  $0.1 \text{ mol L}^{-1}$ , the catalytic activity increased significantly. The geometries and energies for all the intermediates involved in methanol decomposition are analyzed through first-principles DFT valuations, and the most likely reaction pathway of methanol oxidation on NiO(100) is predicted to be  $\text{CH}_3\text{OH} \rightarrow \text{CH}_3\text{O} \rightarrow \text{CH}_2\text{O} \rightarrow \text{CHO} \rightarrow \text{CHOOH} \rightarrow \text{COOH} \rightarrow \text{CO}_2$ .

### **Acknowledgements**

This work was supported by the National Key Research and Development Program of China (No. 2018YFE0202003, 2016YFB0101208) and the Beijing Key Research and Development Program (No.Z181100004518004). SRR, RWC and NYD acknowledge the UK Engineering and Physical Sciences Research Council (EPSRC) for funding (Grant No. EP/S001395/1). This work has used the computational facilities of the Advanced Research Computing at Cardiff (ARCCA) Division, Cardiff University, and HPC Wales. This work also made use of the facilities of ARCHER (<http://www.archer.ac.uk>), the UK's national supercomputing service via the membership of the UK's HEC Materials Chemistry Consortium, which is funded by EPSRC (EP/L000202).

### **Conflicts of interest**

There are no conflicts to declare.

### **References**

- [1] T.H.T. Vu, T.T. Nguyen, T.H. Nguyen, M.D. Nguyen, Q.M. Nguyen, A new method for synthesizing high performance few-layer graphene supported Pt electrocatalysts in methanol and ethanol oxidation, *Electrochim. Acta*, 380 (2021) 16.

- [2] X.A. Teng, A.X. Shan, Y.C. Zhu, R.M. Wang, W.M. Lau, Promoting methanol-oxidation-reaction by loading PtNi nano-catalysts on natural graphitic-nano-carbon, *Electrochim. Acta*, 353 (2020) 9.
- [3] C. Wang, F. Ren, C. Zhai, K. Zhang, B. Yang, D. Bin, H. Wang, P. Yang, Y. Du, Au-Cu-Pt ternary catalyst fabricated by electrodeposition and galvanic replacement with superior methanol electrooxidation activity, *RSC Adv.*, 4 (2014) 57600-57607.
- [4] L. Xiong, X.K. Yang, M.L. Xu, Y.Y. Xu, D.P. Wu, Pt-Ni alloy nanoparticles supported on multiwalled carbon nanotubes for methanol oxidation in alkaline media, *J. Solid State Electrochem.*, 17 (2013) 805-810.
- [5] K.W. Park, J.H. Choi, S.A. Lee, C. Pak, H. Chang, Y.E. Sung, PtRuRhNi nanoparticle electrocatalyst for methanol electrooxidation in direct methanol fuel cell, *J. Catal.*, 224 (2004) 236-242.
- [6] W.L. Li, Z.X. Song, X.H. Deng, X.Z. Fu, J.L. Luo, Decoration of NiO hollow spheres composed of stacked nanosheets with CeO<sub>2</sub> nanoparticles: Enhancement effect of CeO<sub>2</sub> for electrocatalytic methanol oxidation, *Electrochim. Acta*, 337 (2020) 8.
- [7] D.M. Zhang, J.J. Zhang, H.Y. Wang, C. Cui, W.Z. Jiao, J. Gao, Y.Z. Liu, Novel Ni foam based nickel oxalate derived porous NiO nanostructures as highly efficient electrodes for the electrooxidation of methanol/ethanol and urea, *J. Alloy. Compd.*, 806 (2019) 1419-1429.
- [8] A.M. Al-Enizi, M.A. Ghanem, A.A. El-Zatahry, S.S. Al-Deyab, Nickel oxide/nitrogen doped carbon nanofibers catalyst for methanol oxidation in alkaline media, *Electrochim. Acta*, 137 (2014) 774-780.
- [9] M. Asgari, M.G. Maragheh, R. Davarkhah, E. Lohrasbi, Methanol Electrooxidation on the Nickel Oxide Nanoparticles/Multi-Walled Carbon Nanotubes Modified Glassy Carbon Electrode Prepared Using Pulsed Electrodeposition, *J. Electrochem. Soc.*, 158 (2011) K225-K229.
- [10] J.J. Huang, N.W. Zhu, T.T. Yang, T.P. Zhang, P.X. Wu, Z. Dang, Nickel oxide and carbon nanotube composite (NiO/CNT) as a novel cathode non-precious metal catalyst in microbial fuel cells, *Biosens. Bioelectron.*, 72 (2015) 332-339.

- [11] M.B. Askari, P. Salarizadeh, M. Seifi, S.M. Rozati, Ni/NiO coated on multi-walled carbon nanotubes as a promising electrode for methanol electro-oxidation reaction in direct methanol fuel cell, *Solid State Sci.*, 97 (2019) 7.
- [12] R.M.A. Hameed, R.H. Tammam, Nickel oxide nanoparticles grown on mesoporous carbon as an efficient electrocatalyst for urea electro-oxidation, *Int. J. Hydrog. Energy*, 43 (2018) 20591-20606.
- [13] X. Liu, W. Liu, M. Ko, M. Park, M.G. Kim, P. Oh, S. Chae, S. Park, A. Casimir, G. Wu, J. Cho, Metal (Ni, Co)-Metal Oxides/Graphene Nanocomposites as Multifunctional Electrocatalysts, *Adv. Funct. Mater.*, 25 (2015) 5799-5808.
- [14] T.J. Wang, H. Huang, X.R. Wu, H.C. Yao, F.M. Li, P. Chen, P.J. Jin, Z.W. Deng, Y. Chen, Self-template synthesis of defect-rich NiO nanotubes as efficient electrocatalysts for methanol oxidation reaction, *Nanoscale*, 11 (2019) 19783-19790.
- [15] L. Wang, G. Zhang, Y. Liu, W. Li, W. Lu, H. Huang, Facile synthesis of a mechanically robust and highly porous NiO film with excellent electrocatalytic activity towards methanol oxidation, *Nanoscale*, 8 (2016) 11256-11263.
- [16] S.R. Hosseini, S. Ghasemi, M. Karnali-Rousta, S.R. Nabavi, Preparation of NiO nanofibers by electrospinning and their application for electro-catalytic oxidation of ethylene glycol, *Int. J. Hydrog. Energy*, 42 (2017) 906-913.
- [17] C.D. Gu, M.L. Huang, X. Ge, H. Zheng, X.L. Wang, J.P. Tu, NiO electrode for methanol electro-oxidation: Mesoporous vs. nanoparticulate, *Int. J. Hydrog. Energy*, 39 (2014) 10892-10901.
- [18] N.A.M. Barakat, M.A. Abdelkareem, M. El-Newehy, H.Y. Kim, Influence of the nanofibrous morphology on the catalytic activity of NiO nanostructures: an effective impact toward methanol electrooxidation, *Nanoscale Res. Lett.*, 8 (2013).
- [19] G. Kresse, J. Furthmuller, Efficient iterative schemes for ab initio total-energy calculations using a plane-wave basis set, *Phys. Rev. B*, 54 (1996) 11169-11186.
- [20] G. Kresse, AB-INITIO MOLECULAR-DYNAMICS FOR LIQUID-METALS, *J. Non-Cryst. Solids*, 193 (1995) 222-229.
- [21] G. Kresse, D. Joubert, From ultrasoft pseudopotentials to the projector augmented-wave method, *Phys. Rev. B*, 59 (1999) 1758-1775.

- [22] J.P. Perdew, K. Burke, M. Ernzerhof, Generalized gradient approximation made simple (vol 77, pg 3865, 1996), *Phys. Rev. Lett.*, 78 (1997) 1396-1396.
- [23] P.E. Blochl, PROJECTOR AUGMENTED-WAVE METHOD, *Phys. Rev. B*, 50 (1994) 17953-17979.
- [24] S. Grimme, J. Antony, S. Ehrlich, H. Krieg, A consistent and accurate ab initio parametrization of density functional dispersion correction (DFT-D) for the 94 elements H-Pu, *J. Chem. Phys.*, 132 (2010) 19.
- [25] A. Rohrbach, J. Hafner, G. Kresse, Electronic correlation effects in transition-metal sulfides, *J. Phys.-Condes. Matter*, 15 (2003) 979-996.
- [26] B. Himmetoglu, A. Floris, S. de Gironcoli, M. Cococcioni, Hubbard-Corrected DFT Energy Functionals: The LDA + U Description of Correlated Systems, *Int. J. Quantum Chem.*, 114 (2014) 14-49.
- [27] G.W. Watson, E.T. Kelsey, N.H. deLeeuw, D.J. Harris, S.C. Parker, Atomistic simulation of dislocations, surfaces and interfaces in MgO, *J. Chem. Soc.-Faraday Trans.*, 92 (1996) 433-438.
- [28] F. Finocchi, A. Barbier, J. Jupille, C. Noguera, Stability of rocksalt (111) polar surfaces: Beyond the octopole, *Phys. Rev. Lett.*, 92 (2004) 4.
- [29] W.B. Zhang, B.Y. Tang, Stability of the polar NiO(111) surface, *J. Chem. Phys.*, 128 (2008) 5.
- [30] G. Mills, H. Jonsson, G.K. Schenter, REVERSIBLE WORK TRANSITION-STATE THEORY - APPLICATION TO DISSOCIATIVE ADSORPTION OF HYDROGEN, *Surf. Sci.*, 324 (1995) 305-337.
- [31] S.I. Kim, J.S. Lee, H.J. Ahn, H.K. Song, J.H. Jang, Facile Route to an Efficient NiO Supercapacitor with a Three-Dimensional Nanonetwork Morphology, *ACS Appl. Mater. Interfaces*, 5 (2013) 1596-1603.
- [32] Q. Luo, M.Y. Peng, X.P. Sun, A.M. Asiri, Hierarchical nickel oxide nanosheet@nanowire arrays on nickel foam: an efficient 3D electrode for methanol electro-oxidation, *Catal. Sci. Technol.*, 6 (2016) 1157-1161.

- [33] H. Liu, G.X. Wang, J. Liu, S.Z. Qiao, H.J. Ahn, Highly ordered mesoporous NiO anode material for lithium ion batteries with an excellent electrochemical performance, *J. Mater. Chem.*, 21 (2011) 3046-3052.
- [34] M.Q. Yu, S.L. Wang, J.Y. Hu, Z.Y. Chen, Y.H. Bai, L.J. Wu, J.R. Chen, X.X. Weng, Additive-free macroscopic-scale synthesis of coral-like nickel cobalt oxides with hierarchical pores and their electrocatalytic properties for methanol oxidation, *Electrochim. Acta*, 145 (2014) 300-306.
- [35] J.F. Marco, J.R. Gancedo, M. Gracia, J.L. Gautier, E.I. Rios, H.M. Palmer, C. Greaves, F.J. Berry, Cation distribution and magnetic structure of the ferrimagnetic spinel NiCo<sub>2</sub>O<sub>4</sub>, *J. Mater. Chem.*, 11 (2001) 3087-3093.
- [36] J. Zhan, M. Cai, C.F. Zhang, C. Wang, Synthesis of mesoporous NiCo<sub>2</sub>O<sub>4</sub> fibers and their electrocatalytic activity on direct oxidation of ethanol in alkaline media, *Electrochim. Acta*, 154 (2015) 70-76.
- [37] E. Umeshbabu, G.R. Rao, NiCo<sub>2</sub>O<sub>4</sub> hexagonal nanoplates anchored on reduced graphene oxide sheets with enhanced electrocatalytic activity and stability for methanol and water oxidation, *Electrochim. Acta*, 213 (2016) 717-729.
- [38] N. Spinner, W.E. Mustain, Effect of nickel oxide synthesis conditions on its physical properties and electrocatalytic oxidation of methanol, *Electrochim. Acta*, 56 (2011) 5656-5666.
- [39] W. Xing, F. Li, Z.F. Yan, G.Q. Lu, Synthesis and electrochemical properties of mesoporous nickel oxide, *Journal of Power Sources*, 134 (2004) 324-330.
- [40] J.C. Ruiz-Morales, J. Canales-Vazquez, C. Savaniu, D. Marrero-Lopez, W.Z. Zhou, J.T.S. Irvine, Disruption of extended defects in solid oxide fuel cell anodes for methane oxidation, *Nature*, 439 (2006) 568-571.
- [41] J.Y. Zhang, W.W. Li, R.L.Z. Hoye, J.L. MacManus-Driscoll, M. Budde, O. Bierwagen, L. Wang, Y. Du, M.J. Wahila, L.F.J. Piper, T.L. Lee, H.J. Edwards, V.R. Dhanak, K.H.L. Zhang, Electronic and transport properties of Li-doped NiO epitaxial thin films, *J. Mater. Chem. C*, 6 (2018) 2275-2282.

- [42] R.A. Patil, R.S. Devan, J.-H. Lin, Y. Liou, Y.-R. Ma, An efficient methodology for measurement of the average electrical properties of single one-dimensional NiO nanorods, *Sci Rep*, 3 (2013).
- [43] N. Kitchamsetti, M.S. Ramteke, S.R. Rondiya, S.R. Mulani, M.S. Patil, R.W. Cross, N.Y. Dzade, R.S. Devan, DFT and experimental investigations on the photocatalytic activities of NiO nanobelts for removal of organic pollutants, *J. Alloy. Compd.*, 855 (2021) 157337.
- [44] R. Garcia-Muelas, Q. Li, N. Lopez, Density Functional Theory Comparison of Methanol Decomposition and Reverse Reactions on Metal Surfaces, *ACS Catal.*, 5 (2015) 1027-1036.
- [45] S. Lin, D.Q. Xie, H. Guo, Pathways of Methanol Steam Reforming on PdZn and Comparison with Cu, *J. Phys. Chem. C*, 115 (2011) 20583-20589.

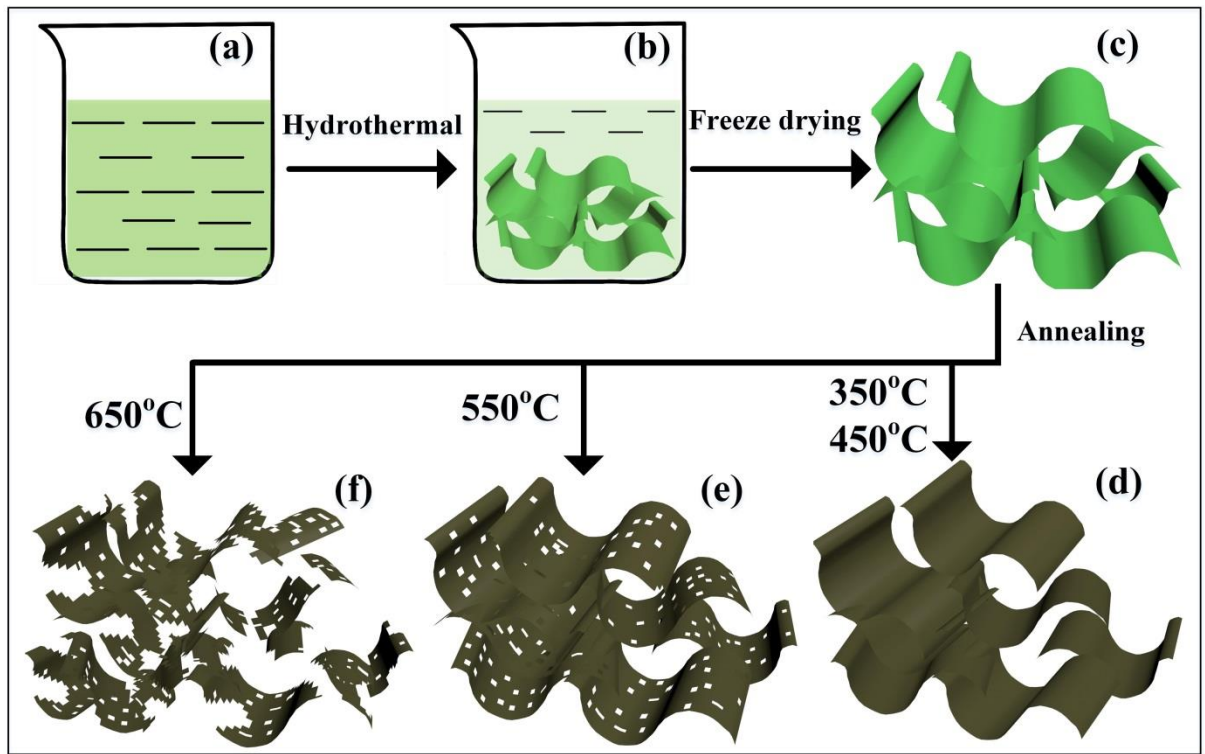


Fig. 1 Synthesis flow diagram of NiO

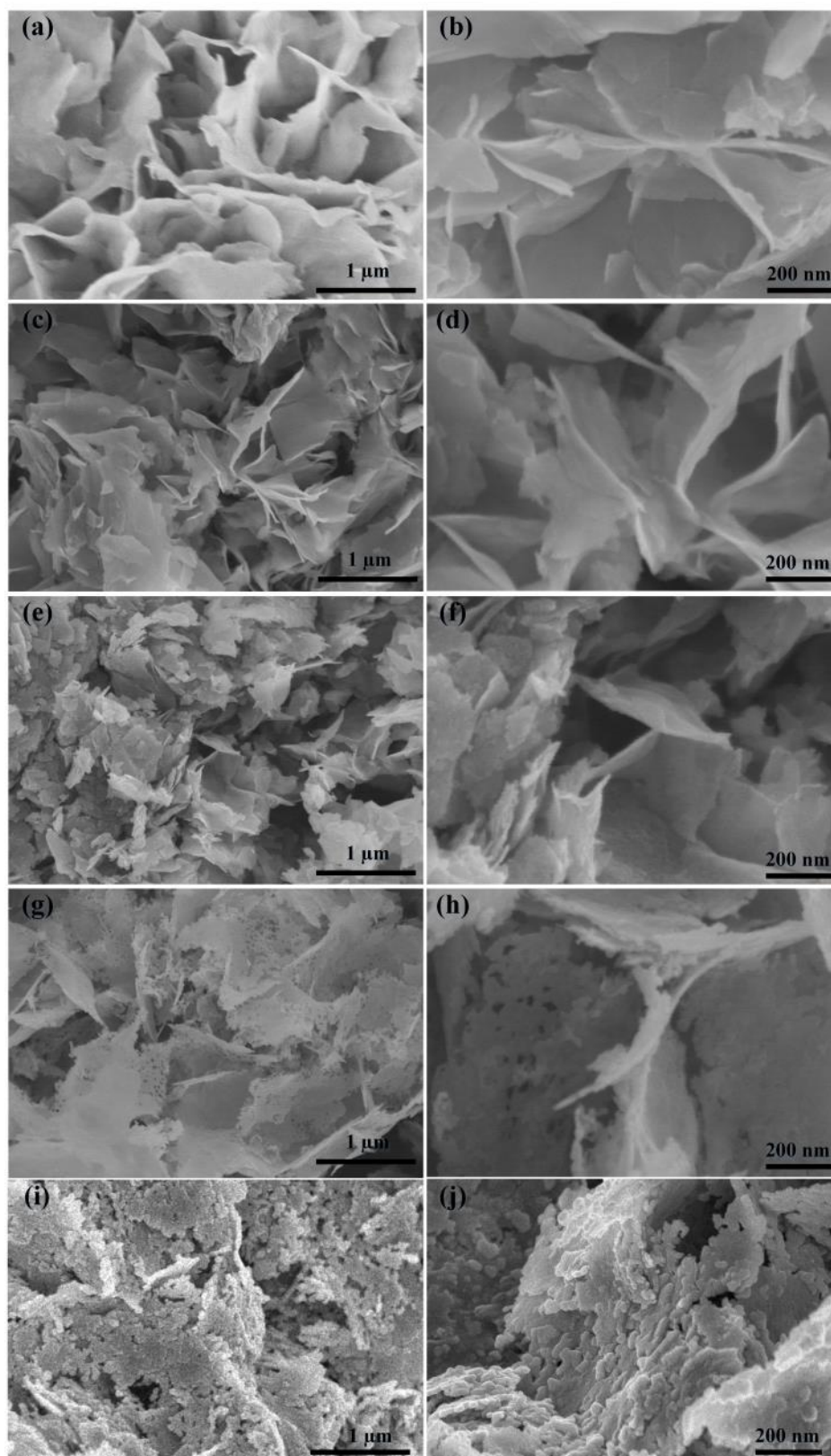


Fig. 2: SEM of (a) and (b)  $\text{Ni}(\text{OH})_2$ ; (c) and (d) 350-NiO; (e) and (f) 450-NiO; (g) and (h) 550-NiO; (i) and (j) 650-NiO.



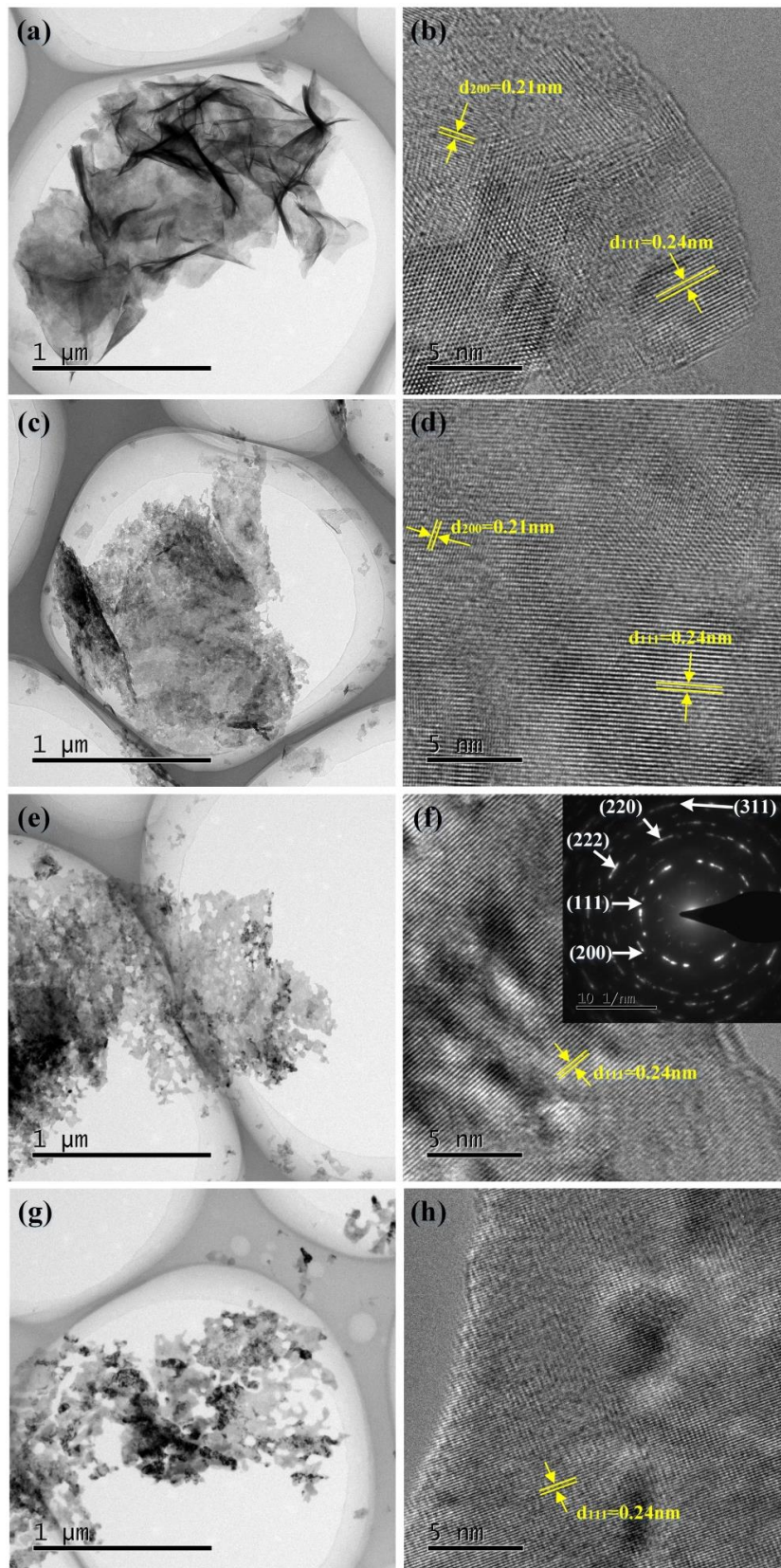


Fig. 3 TEM and HR-TEM images of 350-NiO (a and b); 450-NiO (c and d); 550-NiO (e and f); 650-NiO (g and h). Inset (f) is the 550-NiO with the SAED pattern.

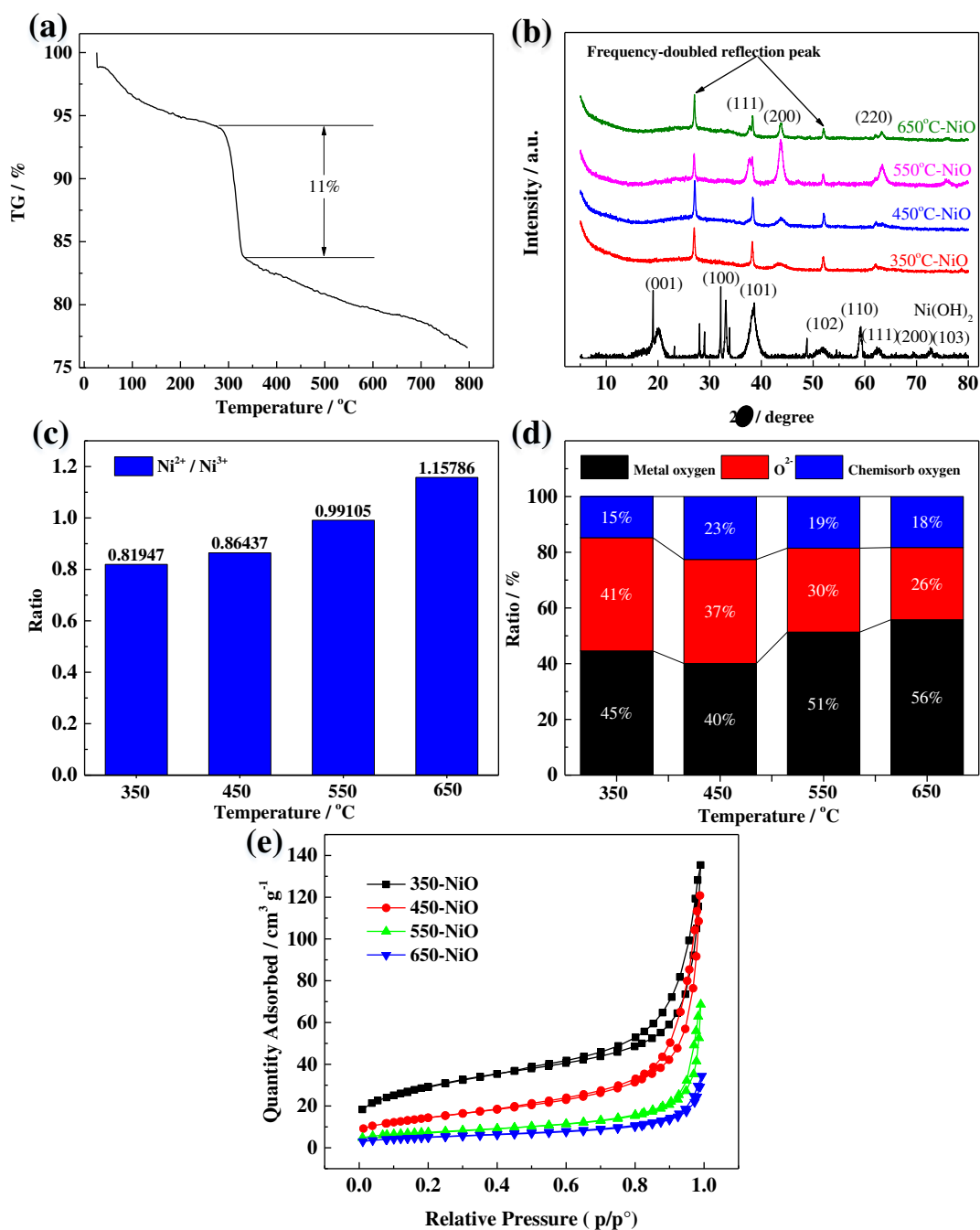


Fig. 4 (a) TGA of NiO-precursor; (b) XRD for NiO-precursor, 350-NiO, 450-NiO, 550-NiO, 650-NiO; (c) comparison of 2-valent and 3-valent for Ni content in XPS analysis of 350-NiO, 450-NiO, 550-NiO, 650-NiO; (d) the comparison of O-containing species for the annealed products of 350-NiO, 450-NiO, 550-NiO, 650-NiO; (e) Nitrogen adsorption/desorption isotherms of 350-NiO, 450-NiO, 550-NiO, 650-NiO.

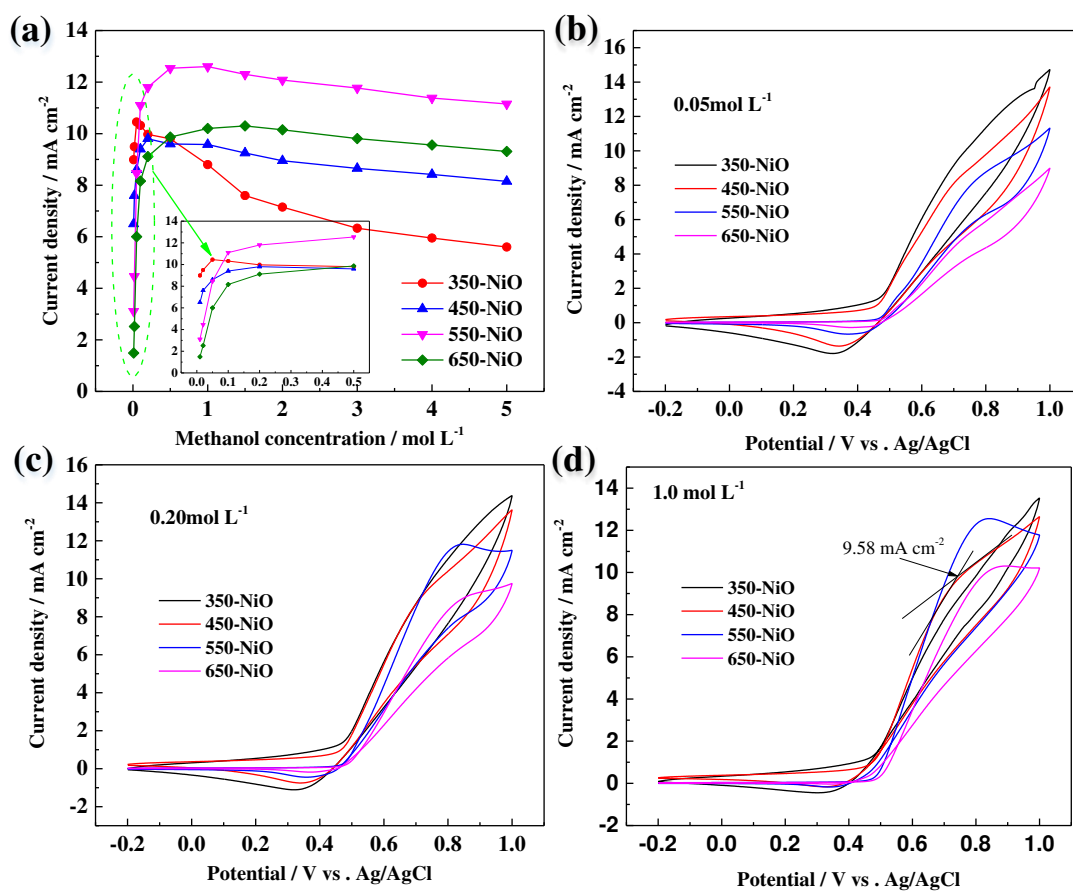


Fig. 5 (a) Comparison of oxidation peaks of methanol at different concentrations, (b) comparison of CV at 0.05 mol L<sup>-1</sup>, (c) comparison of CV at 0.20 mol L<sup>-1</sup>, (d) comparison of CV at 1.0 mol L<sup>-1</sup> of 350-NiO, 450-NiO, 550-NiO, 650-NiO at 50 mV s<sup>-1</sup>.

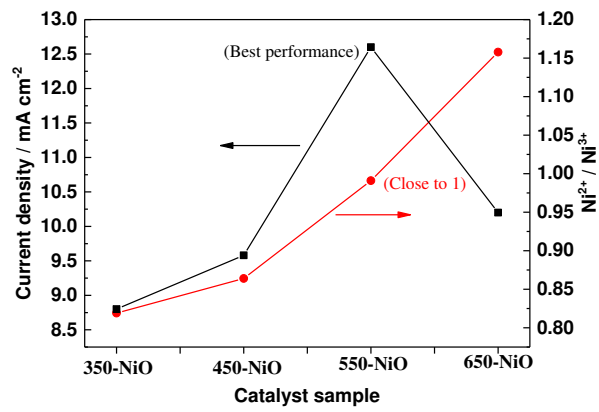


Fig. 6 Relationship between methanol electrocatalytic performance and Ni<sup>2+</sup> / Ni<sup>3+</sup> at methanol concentration of 1.0 mol L<sup>-1</sup>.

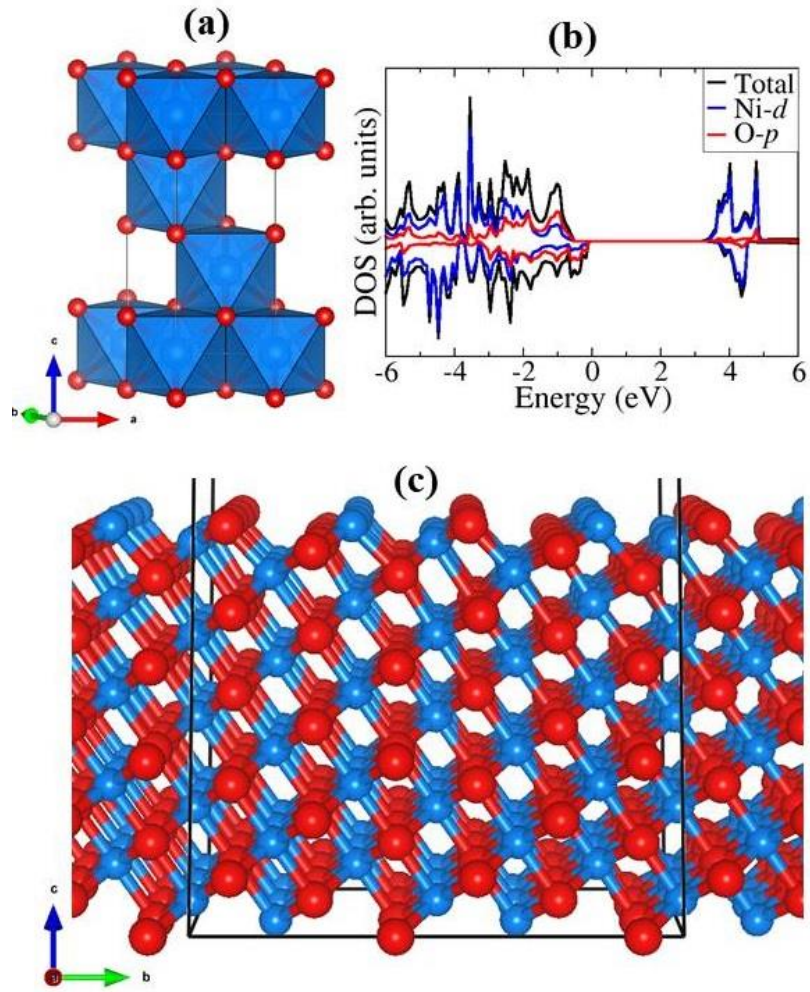


Fig.7 (a) Hexagonal (R-3m) crystal structure, (b) projected density of states (PDOS) of NiO, and (c) optimized structure of NiO(100) surface. Atomic color code: Ni=blue and O=red.



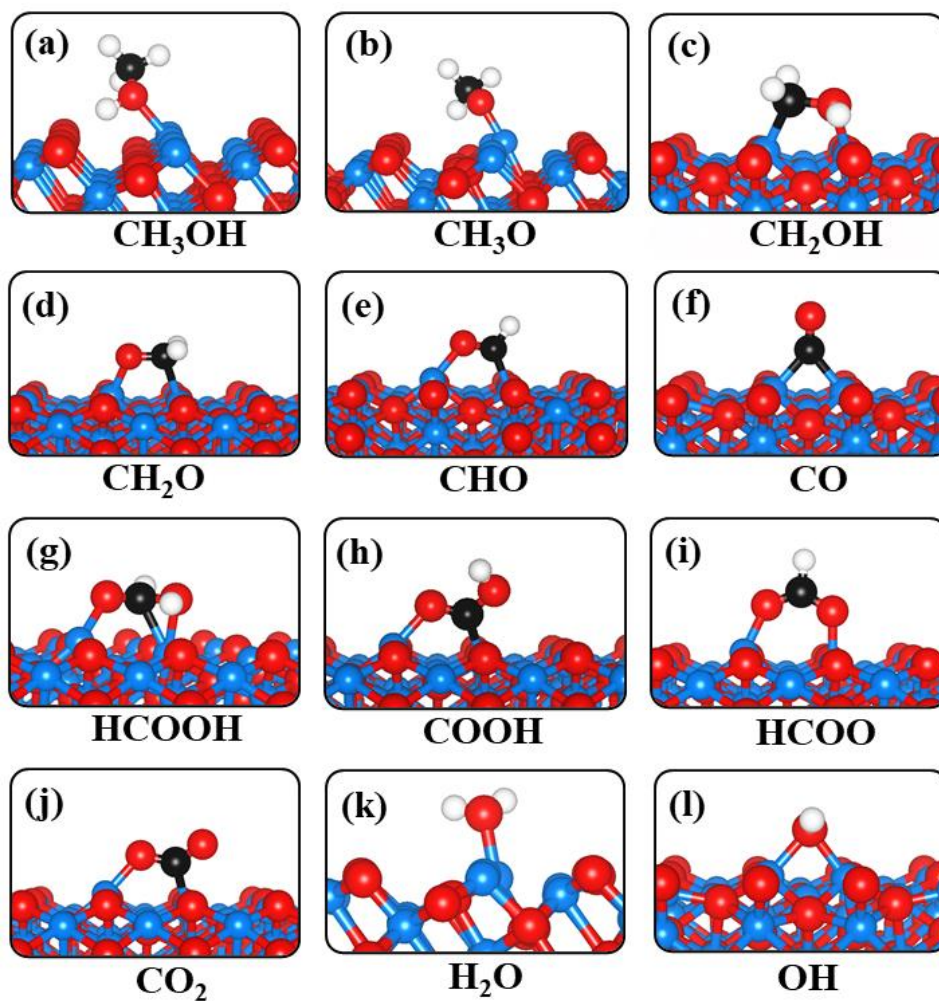


Fig. 8 Optimized structures of the most stable adsorption configurations for the intermediates involved in methanol reaction on NiO(100). Atomic color code: Ni=blue, O=red, C=black, and H=white.

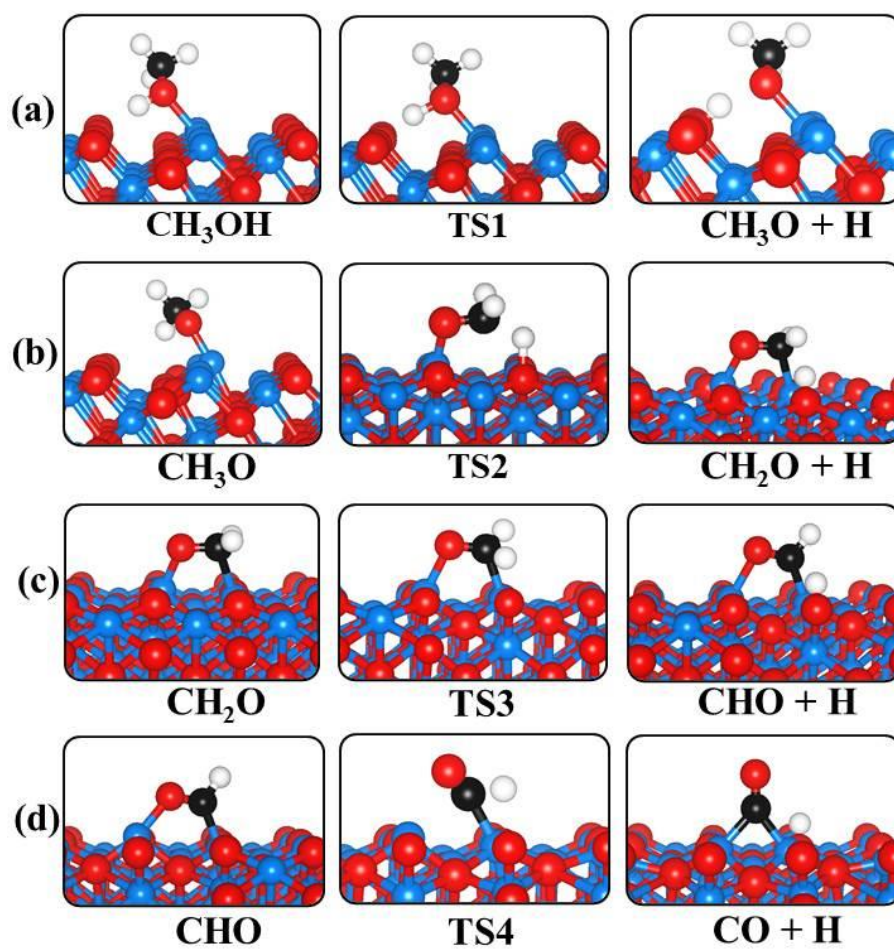


Fig.9 Optimized structures for the initial (left), transition (middle), and final (right) states for the dehydrogenation of methanol via the initial O–H bond scissions on NiO(100). Atomic color code: Ni=blue, O=red, C=black, and H=white.

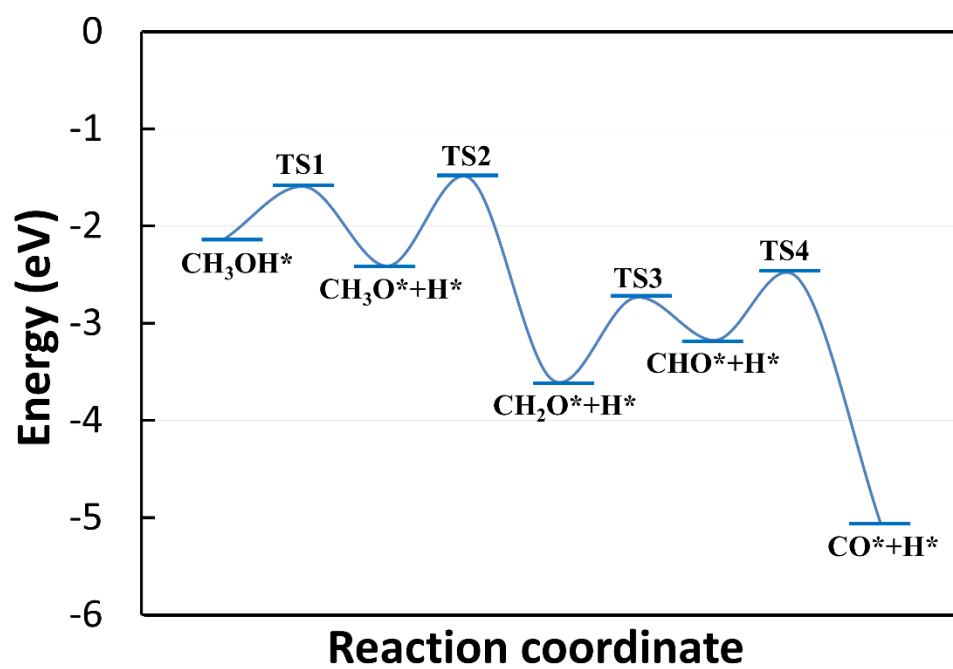


Fig. 10 Energy profile for the dehydrogenation of methanol on NiO(100) surface.



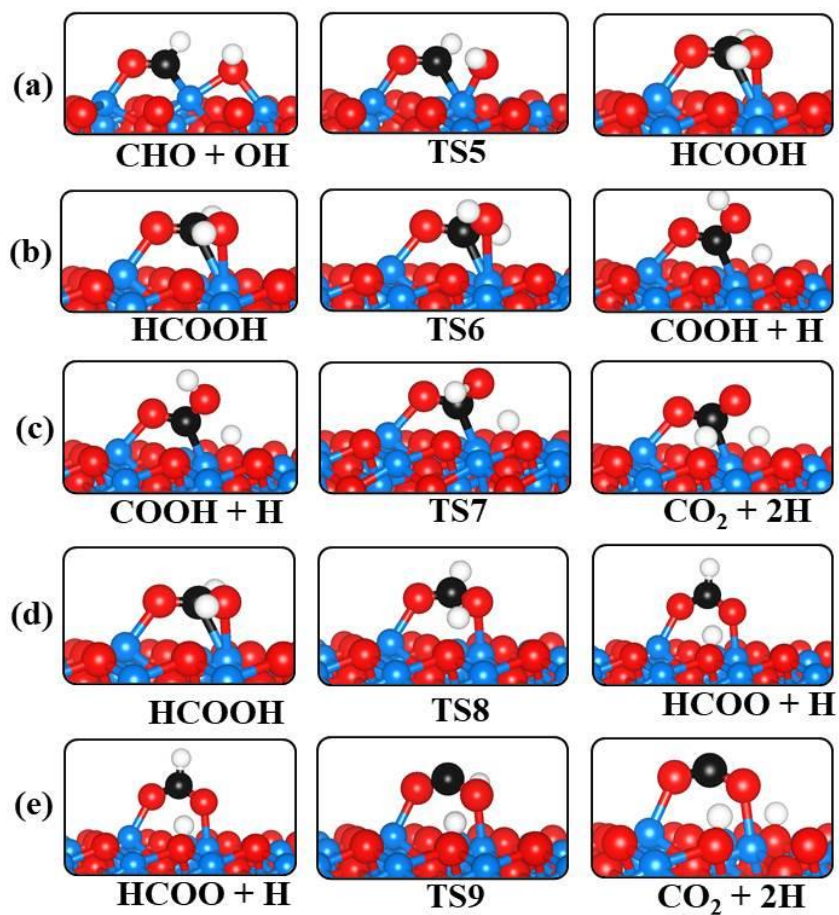


Fig. 11 Optimized structures for the initial (left), transition (middle), and final (right) states for the oxidation of CHO and its decomposition on NiO(100). Atomic color code: Ni=blue, O=red, C=black, and H=white.